Supporting Information

Coupled X-ray Absorption/UV-vis Monitoring of a Prototypical Oscillating Reaction

Francesco Tavani,[†,‡] Federico Frateloreto,[†,‡] Daniele Del Giudice,[†] Giorgio Capocasa,[†] Marika Di Berto Mancini,[†] Matteo Busato,[†] Osvaldo Lanzalunga,[*,†] Stefano Di Stefano,[*,†] and Paola D'Angelo[*,†]

†*Dipartimento di Chimica, Università degli Studi di Roma La Sapienza, P.le A. Moro 5, I-00185 Rome, Italy*

‡*Equal contribution*

E-mail: osvaldo.lanzalunga@uniroma1.it; stefano.distefano@uniroma1.it; p.dangelo@uniroma1.it

1 Materials

1.1 BZ reaction conditions

The BZ reactions were carried out employing a total Ce concentration ($[Ce]_{tot}$) equal to 34.0 mM by mixing malonic acid (MA) (70.0 mM), H_2SO_4 (1.7 M), $NaBrO_3$ (70.2 mM), KBr (5.6 mM) and $Ce(NH_4)_4(SO_4)_4$ (34.0 mM) in aqueous solution at 25 °C. The BZ reactions described in this work were performed in initially homogenized, unstirred solutions. A reaction cell with height, inner width and inner depth dimensions of 52.0 mm, 9.5 mm and 1.0 mm, respectively, was employed for the UV-Vis measurements (Figure S1). The reaction cell used for the XAS data collection was obtained by sealing kapton windows on an aluminum alloy cell with the same dimensions listed above. In a second set of experiments, the BZ reaction was also performed in a quartz capillary (diameter = 1.5 mm and height = 36 mm) and XAS and UV-Vis spectra were collected simultaneously.

2 Methods

2.1 X-ray Absorption measurements

The Br K-edge XAS spectra of the reference compounds and of the BZ reaction conducted in the aluminum alloy cell were collected at room temperature in transmission mode at the Elettra Synchrotron (Trieste, Italy) on the XAFS beamline. The storage ring was operating at 2 GeV with an optimal storage beam current between 300 and 130 mA. The cell was sealed using Kapton film windows of 0.5 mm and the XANES spectra were collected by employing a fast scan mode available at the beamline. The simultaneous XAS/UV-Vis measurements were recorded in transmission mode at the beam-line BM30B French Absorption Spectroscopy Beamline in Material and Environmental Sciences (FAME) at the European Synchrotron Radiation Facility. In this case, the reactions were performed in a capillary which was positioned in order to be crossed orthogonally by the X-ray and UV-Vis beams,

a configuration that did not allow the collection of full XANES spectra with the time resolution required to track the rapid reaction transformations. The storage ring was running in the two-third filling mode with a typical current of 170 mA.

2.2 Decomposition of the Br K-edge XANES data into the spectra and fractional concentrations of key components

XANES spectroscopic measurements of chemical processes yield a series of spectra that may be positioned in a matrix $\boldsymbol{D}$, where the columns of $\boldsymbol{D}$ are the spectra measured at time t. According to Lambert-Beer's law, at any given time a number N of "pure" and independent components weighed by their fractional concentration contributes to the measured signal.[1] Decomposing the experimental data into the spectra associated to the key species and in their relative concentration profiles can offer important insight in the investigated process. In the present work, such decomposition was performed with the PyFitit code,[1] a software that uses to such end an algorithm belonging to the MCR family.

The starting point is the Singular Value Decomposition (SVD) equation:

$$\boldsymbol{D} = \boldsymbol{U} \cdot \boldsymbol{\Sigma} \cdot \boldsymbol{V} + \boldsymbol{E} \tag{1}$$

where the product $\boldsymbol{U} \cdot \boldsymbol{\Sigma}$ contains, on its N columns, a set of values that may be associated to the normalized absorption coefficients, $\boldsymbol{\Sigma}$ is a diagonal matrix known as the *singular values* term, whose elements are sorted in decreasing order, while $\boldsymbol{V}$ can be interpreted as the concentration matrix associated to the N-selected components. Lastly, the error matrix $\boldsymbol{E}$ represents the lack of fit between the experimental data matrix $\boldsymbol{D}$ and the reconstructed matrix $\boldsymbol{\mu} = \boldsymbol{U} \cdot \boldsymbol{\Sigma} \cdot \boldsymbol{V}$. The SVD deconvolution depends on the correct estimation of the number of components N present in the experimental spectral matrix. To this end, in this investigation we evaluated the percentage error committed in reproducing the experimental data with an increasing number N of components, as detailed in the main text, as shown in

Figure S8. The percentage error function has been calculated with the following expression:

$$R(n) = \frac{\sum_{i=1}^{K}\sum_{j=1}^{m}|d_{ij} - \mu_{ij}^{PC=n}|}{\sum_{i=1}^{K}\sum_{j=1}^{m}|d_{ij}|} \times 100 \quad (2)$$

where d_{ij} and $\mu_{ij}^{PC=n}$ are the normalized absorbance values for the dataset and for the dataset reconstructed with N = n, respectively (K and m represent the number of acquired spectra and of the energy points, respectively, while $n = 1, 2, ...K$).

At this point, all matrices in Equation 1 are solely mathematical solutions to the decomposition problem without physico-chemical meaning. Once N is established, the approach implemented by PyFitIt requires the introduction of a transformation N × N matrix $\boldsymbol{T}$ in Equation 1, using the relation $\boldsymbol{I} = \boldsymbol{T} \cdot \boldsymbol{T}^{-1}$:

$$\boldsymbol{D} = \boldsymbol{U} \cdot \boldsymbol{\Sigma} \cdot \boldsymbol{T} \cdot \boldsymbol{T}^{-1} \cdot \boldsymbol{V} + \boldsymbol{E} \quad (3)$$

where the spectra belonging to the key species are given by $\boldsymbol{S} = \boldsymbol{U} \cdot \boldsymbol{\Sigma} \cdot \boldsymbol{T}$ and their concentration profiles by $\boldsymbol{C} = \boldsymbol{T}^{-1} \cdot \boldsymbol{V}$. Subsequently, the matrix elements T_{ij} of matrix $\boldsymbol{T}$ are modified by sliders to achieve $\boldsymbol{S}$ and $\boldsymbol{C}$ which are chemically and physically interpretable. Once this step is achieved, one can finally write:

$$\boldsymbol{D} = \boldsymbol{S} \cdot \boldsymbol{C} + \boldsymbol{E} \quad (4)$$

The unknown number of T_{ij} elements of $\boldsymbol{T}$ is in principle equal to N^2. In order to reduce such ambiguity, the XANES measured on the BrO_3^- and Br^- were constrained to coincide with two of the three extracted components. This operation allows the reduction of the number of unknown T_{ij} elements from N^2 to $N^2 - N$. In our investigation, a 3 × 3 matrix $\boldsymbol{T}$ containing nine elements was employed to retrieve the spectral and concentration profiles of the key species.

The MCR-extracted concentrations of the three main reaction species (Figure 3c of the main text) obtained from the first XAS independent experiment are correlated to the evolution of the intensity variation recorded at E = 13477.4 eV (Figure 4a of the main text) which were measured through XAS during the subsequent coupled XAS/UV-Vis experiment. In particular, the concentration evolution of the BrO_3^- species (dark blue curve in Figure 3c) reaches higher values at about 138, 248 and 318-350 s from reaction start. In turn, the intensity variation recorded at E = 13477.4 eV (purple curve in the top panel of Figure 4a), which during the initial BZ reaction phase may largely be attributed to the changes in concentration of BrO_3^-, decays in a step-like fashion and reaches higher values at about 175, 248, 300 and 345 s from reaction start. There is a very good correspondence between the time scales of the bromate-related patterns observed while performing the two distinct experiments we have reported, and any slight differences may be attributed to the different geometries and dimensions of the employed reactor cells. Finally, we point out that the more clearly defined differences in concentration variations of BrO_3^- shown in Figure 3c if compared to those shown in Figure 4a may well be attributed to the spectral normalization and absorption correction procedures applied solely to the XANES spectra measured during the first independent XAS experiment.

2.3 Determination of the number of principal components through the scree plot statistical test

The Br K-edge spectroscopic data were subjected to the scree plot test in order to assess the number of pure species present in the reaction mixture.

It is possible to demonstrate that:

$$\lambda_i = \frac{\sigma_{ii}^2}{m-1} \tag{5}$$

where σ_{ii} are the singular values extracted by the Singular Value Decomposition procedure and λ_i are the eigenvalues of the covariance matrix of $\mathbf{D}$ (evaluated for m energy steps) relative to every i-th component. These values correspond to the variance of each principal component (PC).[1,2] Consequently, the components with a high σ_{ii} value contribute significantly to the dataset reconstruction, while those with a small σ_{ii} value are associated to noise.

In the scree plot, the singular values relative to each principal component are plotted against the number of PCs. The presence of an elbow in such curve separates the signal and noise related components.

2.4 Mechanistic interpretation of the XAS results

The FKN model of the BZ cerium ion catalyzed reaction is presented in Table 1, while a schematic overview of the FKN reactive processes that involve the BrO_3^-, Br^- and BrMA species is shown in Figure 1a of the main text. In brief, according to this model the reduced and oxidized Ce^{3+} and Ce^{4+} states are dominant at sufficiently low and high Br^- concentration, respectively. When the Ce^{3+} state is dominant, the reaction proceeds towards MA bromination and Br^- removal, with BrO_3^- being reduced by Br^- to Br_2 via $HBrO_2$ and HOBr (processes R1–R3 in Table 1 of the main text). Once the Br^- concentration has decreased below a critical value $[Br^-]_{cr}$, the system switches to a state with high concentration of the $HBrO_2$ and Ce^{4+} species, through autocatalytic production of $HBrO_2$ (processes R4–R5 in Table 1) whose concentration is then depleted and therefore reaches a steady state without exponential growth. The FKN mechanism is Br^-–controlled since in this model the reverse switch from Ce^{4+} to Ce^{3+} occurs mainly because of the regeneration of the Br^- ion due to the oxidation of the bromomalonate (BrMA) species by Ce^{4+} (process R10 in Table 1).[3,4]

The observed general concentration trends for the three main reagents obtained from the PCA analysis of the XAS spectra may be interpreted as follows. Let v_1 and v_4 be the forward

rates of processes R1 and R4 in the FKN mechanism (Table 1), and v_8 and v_{10} those of processes R8 and R10. As previously noted,[5] application of the steady state approximation to the $BrO_2^{\bullet}$ and $HBrO_2$ concentrations leads to the following expressions for the time evolution of the concentrations of BrO_3^- and BrMA:

$$\frac{\mathrm{d}[BrO_3^-]}{\mathrm{dt}} = -v_1 - v_4 \tag{6}$$

$$\frac{\mathrm{d}[BrMA]}{\mathrm{dt}} = +v_8 - v_{10} \tag{7}$$

According to Eq. 6, overall, the concentration of BrO_3^- decreases during the BZ reaction. However, the Ce^{4+}/Ce^{3+} concentration oscillations induce an oscillation also of the BrO_3^- concentration that is detectable when the $[Ce]_{tot}$ is sufficiently high, as in our experimental conditions, and is coupled to that of BrMA. Note that the amplitudes of both the BrO_3^- and BrMA concentration oscillations highlighted by the XAS measurements and that of Ce^{4+} determined by the UV-Vis measurements fade out with very similar time evolution. Conversely, in Eq. 7 there are two terms with opposite sign.[5] The observed concentration evolution of the BrMA species may be explained by assuming the predominance of process R8 during phases A and B, and that of process R10 during phase C of the reaction. Within this picture, v_8 is greater than v_{10} during the reaction stages A and B and an overall increase in BrMA concentration is observed, while during stage C, also due to the accumulation of BrMA, v_{10} becomes greater than v_8 and the consequent BrMA decarboxylation leads to a conversion of BrMA to Br^-. In turn, the relative concentration of Br^- remains very low during stages A and B and increases during stage C due to process R10 (Figure S4c, purple curve). This behaviour is consistent with previous experimental and theoretical studies[5,6] that reported Br^- concentration oscillations in the order of 1×10^{-6} M that is below the sensitivity of our combined XAS-MCR technique. Finally, although the initial concentration of Br^- is ca. 7% of the total bromine present in the reaction mixture ($[KBr]_0 = 5.6$ mM), no

Br^- could be detected in the first XAS spectrum recorded at $t = 2.30$ min as it has already evolved according to processes R1–R3.

2.5 Kinetic model

2.5.1 Oregonator model

The Oregonator model employed in this work uses the 5 basic reactions listed in Table S1. In this simplified model five coupled reactions are considered, as shown in Table S1, where the rate constants are defined on the basis of the associated FKN rate constants and step O5 is governed by the adjustable stoichiometric factor f.[7–10] In order to replicate the experimentally observed decrease in BrO_3^- concentration, in the employed kinetic model a system of five nonlinear differential equations was solved for the concentrations of the reactants BrO_3^-, Ce^{4+}, $HBrO_2$, Br^- and MA, while assuming that H^+ and HOBr concentrations remain unchanged during the reaction (see the SI for full details).[10] Table S2 lists the initial concentrations of the Oregonator species which were kept equal to those employed in the previously discussed BZ experiments, with the exception of those of Ce^{4+} and Br^- that were set equal to 3.0 mM and 1.5 mM, respectively, i.e. to catalytic concentration values in the 1.0–3.0 mM range, in line with previous Oregonator studies.[10]

Table S1: Employed Oregonator reaction scheme.

Step	Reaction	Rate Constant	Rate Constant values
O1	$BrO_3^- + 2\,H^+ + Br^- \longrightarrow HBrO_2 + HOBr$	$k_1 = k_{R1}[H^+]^2$	2 mol^{-3} dm^9 s^{-1}
O2	$HBrO_2 + H^+ + Br^- \longrightarrow 2\,HOBr$	$k_2 = k_{R2}[H^+]$	10^6 mol^{-2} dm^6 s^{-1}
O3	$BrO_3^- + HBrO_2 + H^+ \longrightarrow 2\,HBrO_2 + Ce^{4+}$	$k_3 = k_{R4}[H^+]$	10 mol^{-2} dm^6 s^{-1}
O4	$2\,HBrO_2 \longrightarrow BrO_3^- + HOBr + H^+$	$k_4 = k_{R6}[H^+]$	2000 mol^{-1} dm^3 s^{-1}
O5	$Ce^{4+} + CH_2(COOH)_2 \longrightarrow f \cdot Br^-$	k_5	1 mol^{-1} dm^3 s^{-1}

The initial concentrations of the reagents and of the catalyst are shown in Table S2 below. The adjustable stoichiometric factor f was set equal to a 0.6 value.

Table S2: Initial concentration of the reagents and catalyst in the employed Oregonator model.

$[BrO_3^-]/(M)$	$[CH_2(COOH)_2]/(M)$	$[Br^-]/(M)$	$[Ce^{4+}]/(M)$	$[H^+]/(M)$
0.0702	0.070	0.0015	0.003	1.75

The following system of five nonlinear differential equations was solved:[6,10,11]

$$\frac{\mathrm{d}[HBrO_2]}{\mathrm{dt}} = k_1[BrO_3^-][Br^-][H^+]^2 - k_2[HBrO_2][Br^-][H^+] + k_3[BrO_3^-][HBrO_2][H^+] - 2k_4[HBrO_2]^2 \tag{8}$$

$$\frac{\mathrm{d}[Br^-]}{\mathrm{dt}} = -k_1[BrO_3^-][Br^-][H^+]^2 - k_2[HBrO_2][Br^-][H^+] + fk_5[Ce^{4+}][CH_2(COOH)_2]_{const} \tag{9}$$

$$\frac{\mathrm{d}[Ce^{4+}]}{\mathrm{dt}} = k_3[BrO_3^-][HBrO_2][H^+] - k_5[Ce^{4+}][CH_2(COOH)_2] \tag{10}$$

$$\frac{\mathrm{d}[BrO_3^-]}{\mathrm{dt}} = -k_1[BrO_3^-][Br^-] - k_3[Ce^{4+}][CH_2(COOH)_2] + 2k_4[HBrO_2]^2 \tag{11}$$

$$\frac{[CH_2(COOH)_2]}{\mathrm{dt}} = -k_5[Ce^{4+}][CH_2(COOH)_2] \tag{12}$$

The $[H^+]$ value was kept fixed to its initial value throughout the simulation. We note that for numerical stability reasons, $[CH_2(COOH)_2]_{const}$ was kept fixed to a value of 0.070 M in Equation 9.

2.5.2 Generation of Chemical Waves

The Oregonator model presented above was employed to simulate the two-dimensional space-time evolution of chemical waves. The system of the five variable dynamic equations may be expressed as follows:

$$\begin{cases} \frac{\mathrm{d}[\mathrm{HBrO_2}]}{\mathrm{dt}} = f_1([\mathrm{HBrO_2}],\, [\mathrm{BrO_3^-}],\, [\mathrm{Br^-}],\, [\mathrm{Ce^{4+}}],\, [\mathrm{CH_2(COOH)_2}]) \\ \frac{\mathrm{d}[\mathrm{BrO_3^-}]}{\mathrm{dt}} = f_2([\mathrm{HBrO_2}],\, [\mathrm{BrO_3^-}],\, [\mathrm{Br^-}],\, [\mathrm{Ce^{4+}}],\, [\mathrm{CH_2(COOH)_2}]) \\ \frac{\mathrm{d}[\mathrm{Br^-}]}{\mathrm{dt}} = f_3([\mathrm{HBrO_2}],\, [\mathrm{BrO_3^-}],\, [\mathrm{Br^-}],\, [\mathrm{Ce^{4+}}],\, [\mathrm{CH_2(COOH)_2}]) \\ \frac{\mathrm{d}[\mathrm{Ce^{4+}}]}{\mathrm{dt}} = f_4([\mathrm{HBrO_2}],\, [\mathrm{BrO_3^-}],\, [\mathrm{Br^-}],\, [\mathrm{Ce^{4+}}],\, [\mathrm{CH_2(COOH)_2}]) \\ \frac{\mathrm{d}[\mathrm{CH_2(COOH)_2}]}{\mathrm{dt}} = f_5([\mathrm{HBrO_2}],\, [\mathrm{BrO_3^-}],\, [\mathrm{Br^-}],\, [\mathrm{Ce^{4+}}],\, [\mathrm{CH_2(COOH)_2}]) \end{cases}$$

(13)

The five-variable reaction-diffusion equations for the BZ reaction components were derived by applying Fick's law and the continuity equation of incompressible fluids. In the case of $[\mathrm{Br^-}]$ we wrote:

$$\frac{\partial [Br_-]}{\partial \mathrm{t}} = D_{Br^-}\frac{\partial^2[\mathrm{Br^-}]}{\partial x^2} + \frac{\partial^2[\mathrm{Br^-}]}{\partial y^2} + f_3 = D_{Br^-}\nabla^2[\mathrm{Br^-}] + f_3 \qquad (14)$$

where D_{Br^-} and $\nabla^2[\mathrm{Br^-}]$ represent the diffusion coeffient of $\mathrm{Br^-}$ in the aqueous medium and a Laplace operator, respectively. The ensuing system of differential equations may be solved using a nine-point Finite Difference (FD) method, which we briefly discuss below.[12,13] The aim of the FD method is to discretize the Laplace operator and time part contained in Equation 14. As has been previously demonstrated,[13] the Laplace operator may be discretized as follows:

$$(\frac{\partial^2[\mathrm{Br}^-]}{\partial \mathrm{i}^2}+\frac{\partial^2[\mathrm{Br}^-]}{\partial \mathrm{j}^2})=\frac{1}{(\delta x)^2}(-[\mathrm{Br}^-]_{i-2,j}+16[\mathrm{Br}^-]_{i-1,j}-60[\mathrm{Br}^-]_{i,j}+16[\mathrm{Br}^-]_{i+1,j} \\ -[\mathrm{Br}^-]_{i+2,j}-[\mathrm{Br}^-]_{i,j-2}+16[\mathrm{Br}^-]_{i,j-1}+16[\mathrm{Br}^-]_{i,j+1}-[\mathrm{Br}^-]_{i,j+2}+o((\delta x)^4)) \tag{15}$$

where δx is the space step and where i, j represent the nodes in the x, y plane of the two-dimensional grid on which the wave diffusion is followed (e.g., $[\mathrm{Br}^-]_{i,j}$ is the concentration of Br^- at the node i, j of the grid, while $\mathrm{Br}^-]_{i,j+2}$ is that of Br^- at the node $i, j+2$, etc.). Conversely, the time part in Equation 14 may be discretized as:

$$\frac{\partial[\mathrm{Br}^-]}{\partial \mathrm{t}}=\frac{[\mathrm{Br}^-]^{t+1}-[\mathrm{Br}^-]^t}{\Delta \mathrm{t}}+\frac{\Delta \mathrm{t}}{2}\frac{\partial^2[\mathrm{Br}^-]^k}{\partial \mathrm{t}^2}, t<k<t+\Delta \mathrm{t} \tag{16}$$

where Δt is the time step, and where $[\mathrm{Br}^-]^{t+1}$ and $[\mathrm{Br}^-]^t$ are the concentrations of the Br^- species at the time steps $t+1$ and t. By substituting Equations 15 and 16 into Equation 14, it is possible to derive[12,13] the algebraic rule by which $[\mathrm{Br}^-](\mathrm{x}_i,\mathrm{y}_i)^{t+1}$, i.e. the concentration of Br^- at a node with x_i, y_i coordinates and at a given time step $t+1$, is iteratively updated by employing the concentration of BrO^- at the nodes in the vicinity of x_i, y_i and at the previous time step t. Specifically, in this approach $[\mathrm{Br}^-](\mathrm{x}_i,\mathrm{y}_i)^{t+1}$ depends on the nine terms: $\{[\mathrm{Br}^-](\mathrm{x}_i,\mathrm{y}_i)^t$, $[\mathrm{Br}^-](\mathrm{x}_{i-2},\mathrm{y}_i)^t$, $[\mathrm{Br}^-](\mathrm{x}_{i-1},\mathrm{y}_i)^t$, $[\mathrm{Br}^-](\mathrm{x}_{i+1},\mathrm{y}_i)^t$, $[\mathrm{Br}^-](\mathrm{x}_{i+2},\mathrm{y}_i)^t$, $[\mathrm{Br}^-](\mathrm{x}_i,\mathrm{y}_{i-2})^t$, $[\mathrm{Br}^-](\mathrm{x}_i,\mathrm{y}_{i-1})^t$, $[\mathrm{Br}^-](\mathrm{x}_i,\mathrm{y}_{i+1})^t$, $[\mathrm{Br}^-](\mathrm{x}_i,\mathrm{y}_{i+2})^t\}$. We note that the numerical values of D_{Br^-} and of the space and time steps have been chosen in order to ensure the oscillatory behaviour and the stability of the target waves. We refer the reader to the work, for instance, of Ai et al.[14] for additional details on the convergence procedures and on the format stability of the employed FD scheme.

3 Supplementary Figures S1–S11

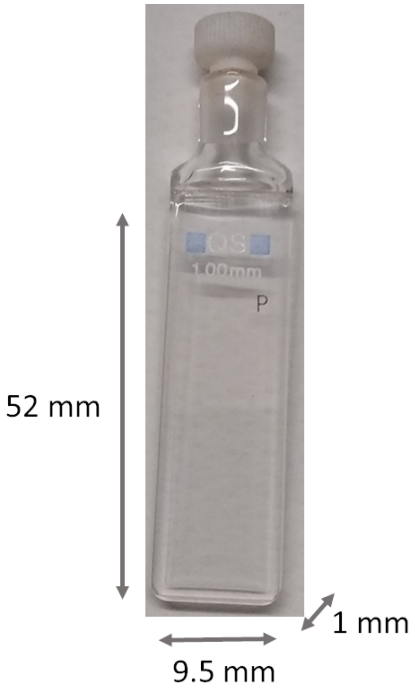

Figure S1: Image of the cell employed in this study to monitor the BZ reaction through UV-Vis spectroscopy. The inner dimensions of the cell are listed. An Aluminum alloy cell with same dimensions and Kapton windows was employed to monitor the BZ reaction through XAS.

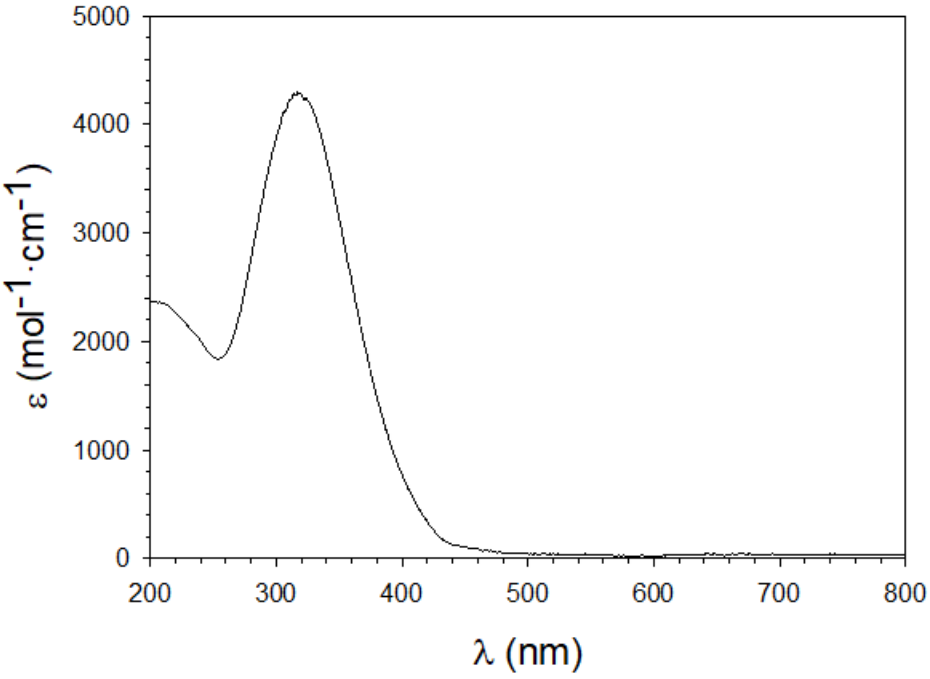

Figure S2: UV-Vis spectrum of $(NH_4)_4Ce(SO_4)_4 \cdot 2H_2O$ in a 2M aqueous H_2SO_4 solution.

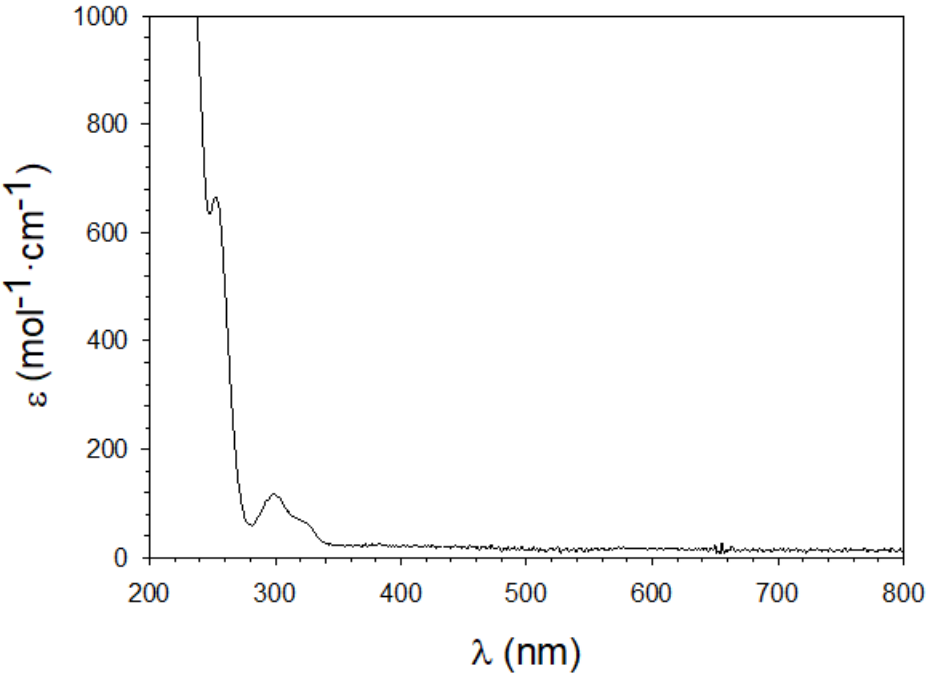

Figure S3: UV-Vis spectrum of $Ce(NO_3)_3{\cdot}6H_2O$ in a 2M aqueous H_2SO_4 solution.

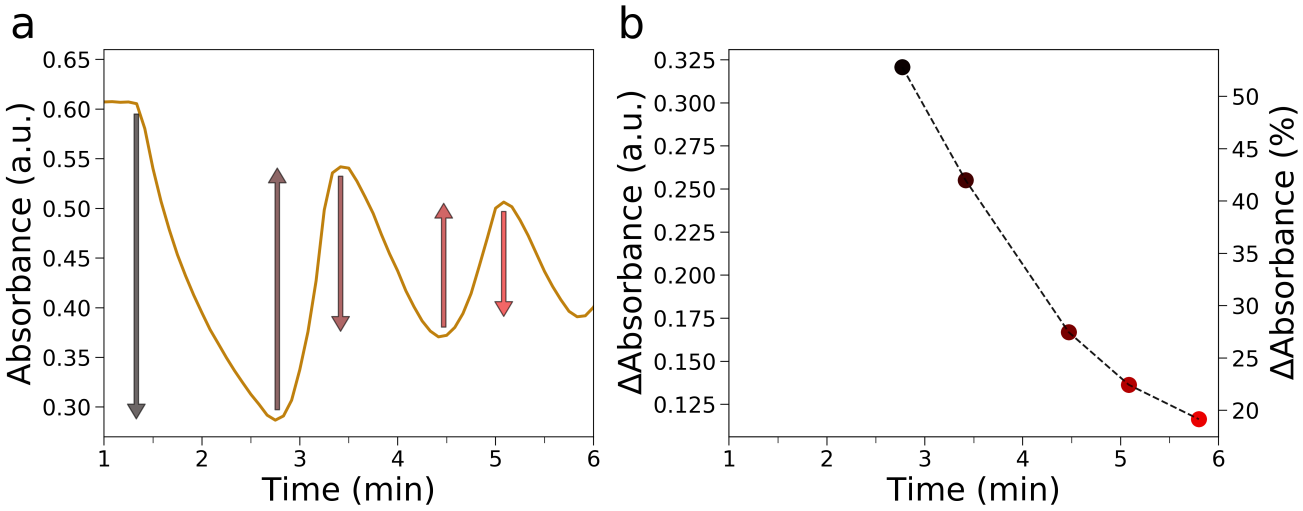

Figure S4: (a) UV-Vis monitoring at $\lambda = 420$ nm of a BZ reaction involving MA (70 mM), H_2SO_4 (1.75 M), $NaBrO_3$ (70.2 mM), KBr (5.6 mM) and $Ce(NH_4)_4(SO_4)_4$ (34 mM). The UV-Vis data coincides with that shown in Figure 1 of the main text, and the time window is restricted to the first six minutes of the reaction. Vertical arrows indicate the main absorbance increases and decays. (b) Time evolution of the absolute and percentage ΔAbsorbance evaluated as the length of the corresponding arrows in panel a.

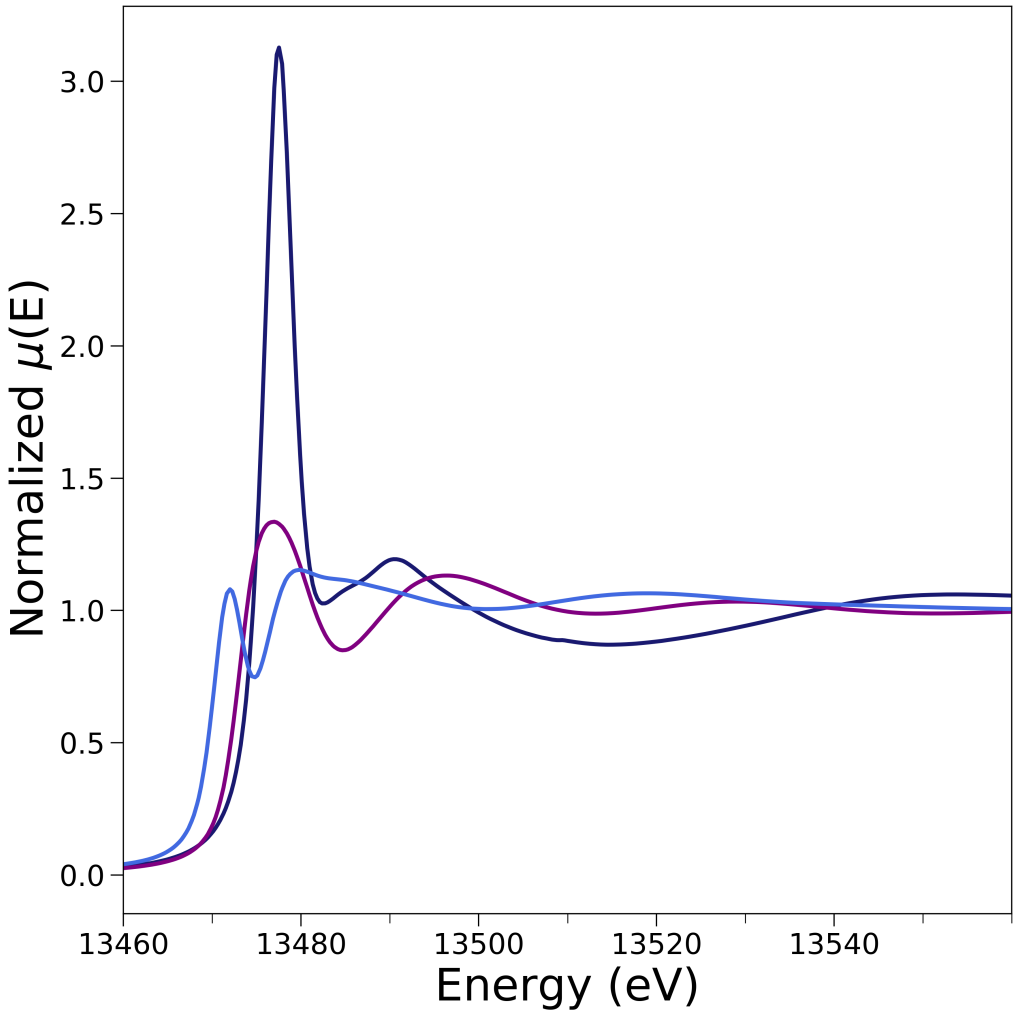

Figure S5: Br K-edge XAS spectra of $NaBrO_3$ 0.1 M (dark blue line) and KBr 0.1 M (purple line) aqueous solutions and of a diethyl bromomalonate 0.1 M (light blue line) methanol solution.

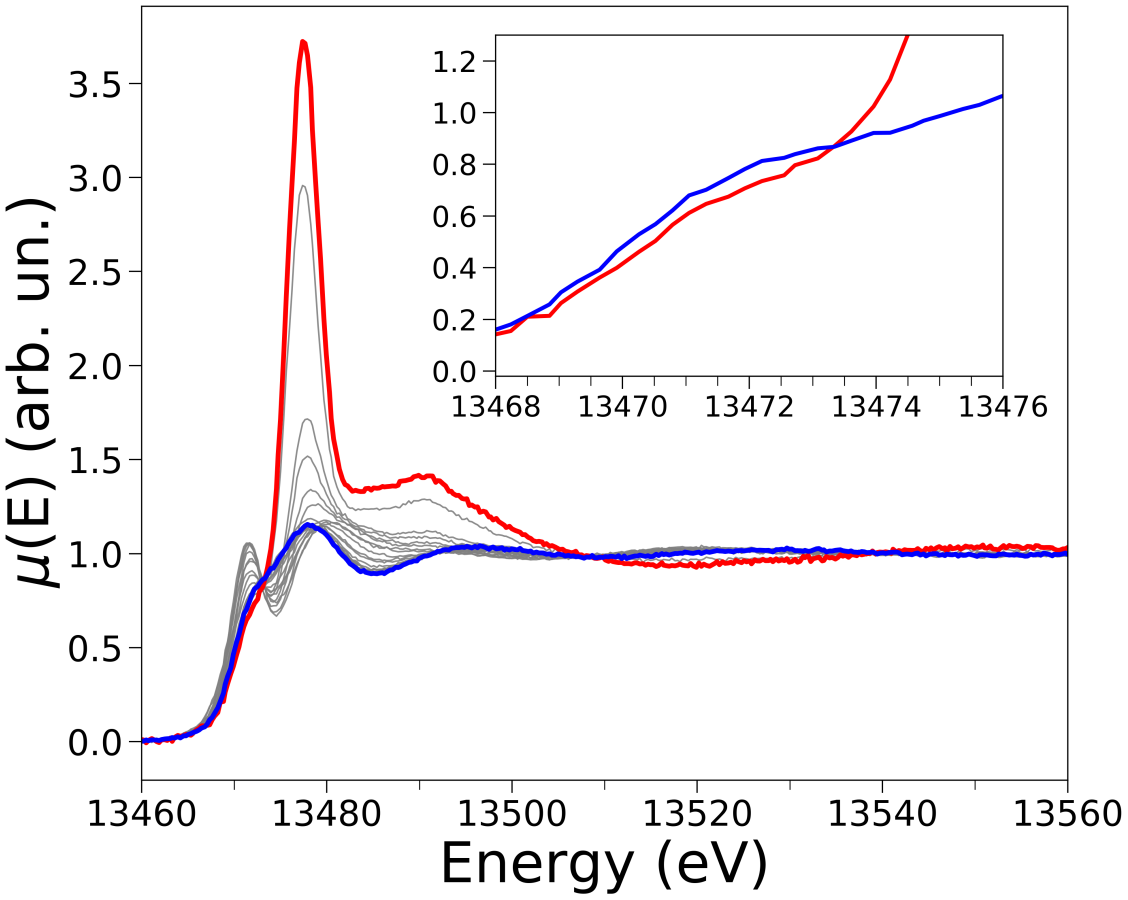

Figure S6: Time evolution of the Br K-edge XANES spectra of the BZ reaction involving MA (70 mM), H_2SO_4 (1.75 M), $NaBrO_3$ (70.2 mM), KBr (5.6 mM) and $Ce(NH_4)_4(SO_4)_4$ (34 mM). The spectroscopic data is portrayed in 2D and corresponds to the 3D XANES spectra shown in Figure 3a of the main text. The first and last recorded XANES spectra are evidenced in red and blue colors, respectively. An enlargement of the pre-edge region of the first and last measured XANES spectra is shown in the inset.

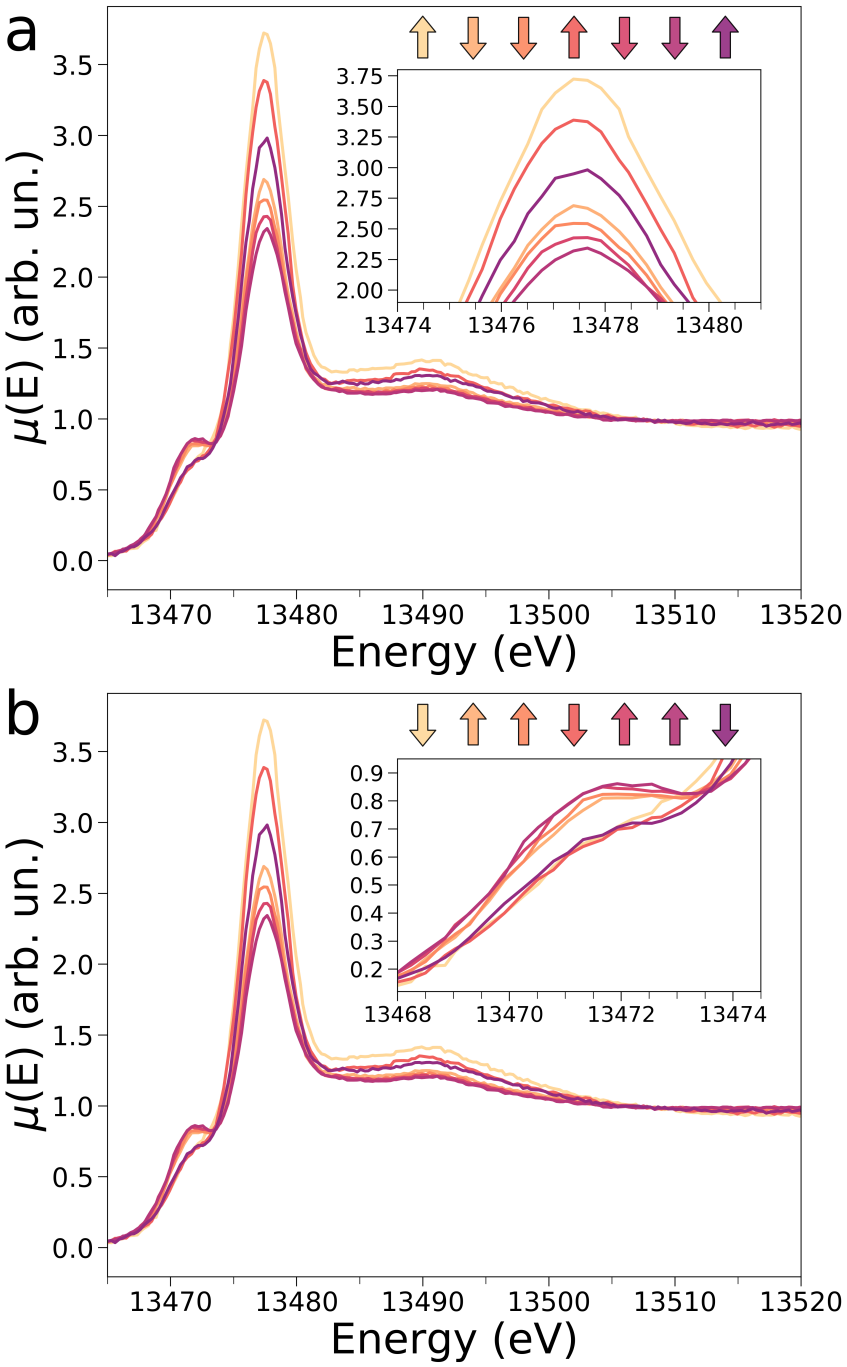

Figure S7: Time evolution of the Br K-edge XANES spectra of the BZ reaction involving MA (70 mM), H_2SO_4 (1.75 M), $NaBrO_3$ (70.2 mM), KBr (5.6 mM) and $Ce(NH_4)_4(SO_4)_4$ (34 mM). The spectroscopic data is portrayed in 2D and corresponds to the 3D XANES spectra shown in Figure 3b of the main text. An enlargement of the white line and of the pre-edge regions is shown in the insets of panels a and b, respectively. In both panels "up" and "down" arrows indicate the experimental intensity increase and decrease, respectively, of the white line and of the pre-edge features in the XANES spectra. In both panels, the XANES spectra color code corresponds to that of the associated arrows. The arrows are ordered from left to right according to the time from reaction start.

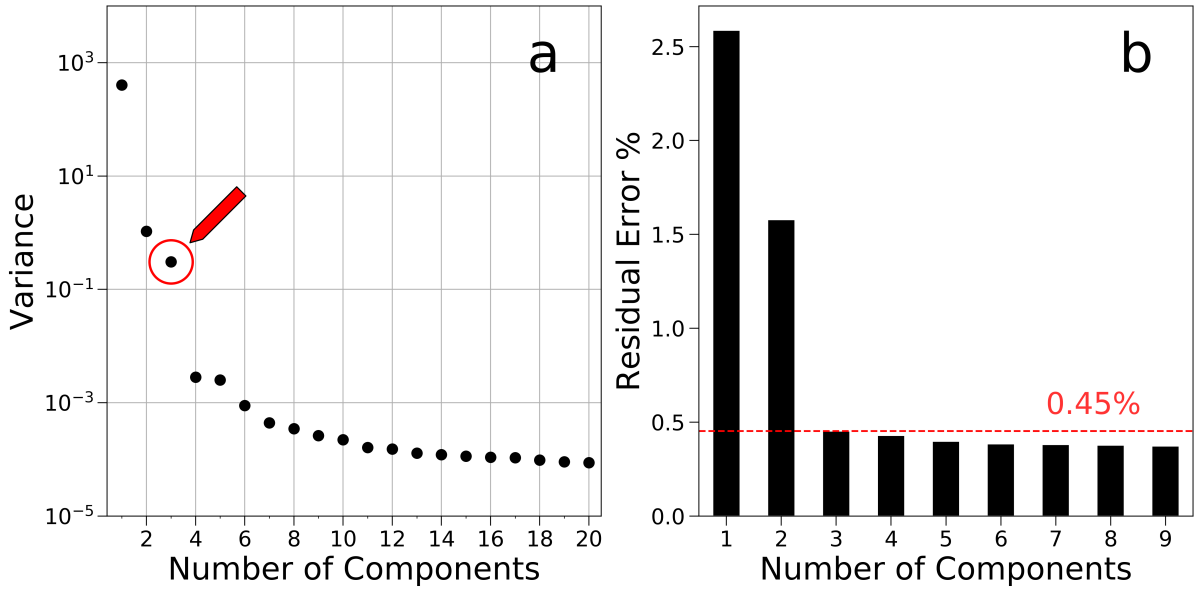

Figure S8: Statistical analysis of the Br K-edge XAS data. Scree plot (a) and percentage error committed in reconstructing the XAS spectra as a function of increasing number of components (b). In panel (a), a red arrow indicates the number (N) of principal components necessary to reproduce the XAS data suggested by the scree plot test, i.e. $N = 3$. In panel (b) the percentage error value committed in reproducing the data using 3 components is evidenced to aide the reader in the visualization.

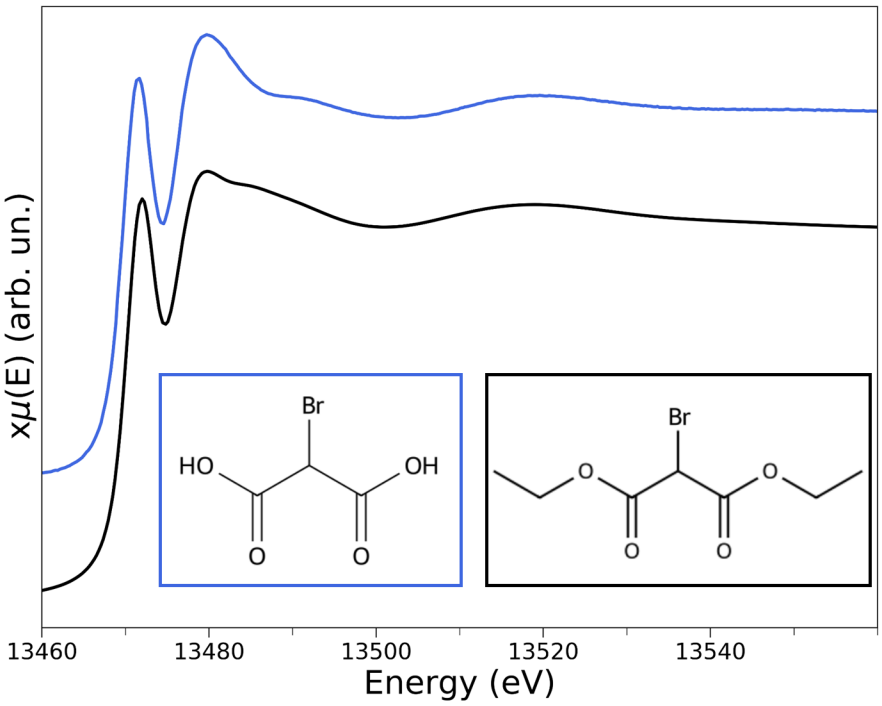

Figure S9: Br K-edge XAS spectra of the reaction intermediate component assigned to the BrMA species (light blue line) and of the diethyl bromomalonate 0.1 M methanol solution (black line). The molecular structures of BrMA and diethyl bromomalonate are shown in the insets.

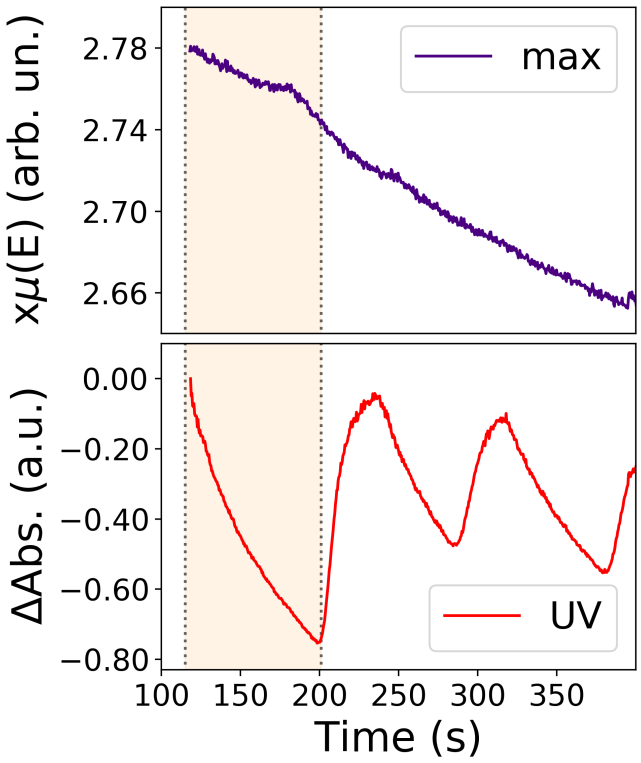

Figure S10: Simultaneous coupled XAS/UV-Vis monitoring of the BZ reaction involving MA (70 mM), H_2SO_4 (1.75 M), $NaBrO_3$ (70.2 mM), KBr (5.6 mM) and $Ce(NH_4)_4(SO_4)_4$ (34 mM). The intensity variation recorded at an energy in proximity of that of the white line (E = 13477.4 eV) measured through XAS (top panel, purple line) and the ΔAbsorbance recorded at $\lambda = 420$ nm (bottom panel, red line) are presented.

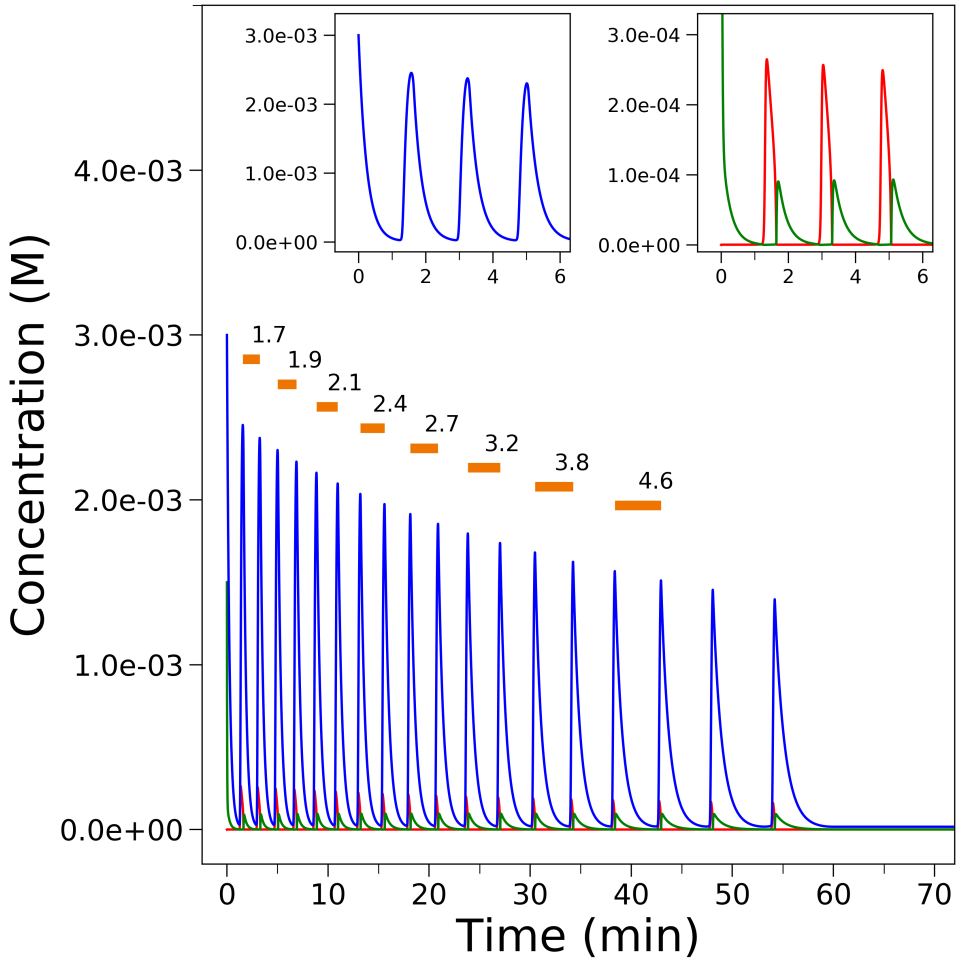

Figure S11: Concentration time evolution of Ce^{4+} (blue), $HBrO_2$ (red) and Br^- (green) derived from the Oregonator model of the BZ reaction presented in this work. The time periods (expressed in minutes) of representative oscillations are listed. Enlargements of the reactant and catalyst concentraton evolution in the first 6 minutes from reaction start are shown in the insets. Initial concentrations: $[BrO_3^-]_0 = 70.2$ mM; $[CH_2(COOH)_2]_0 = 70$ mM; $[Br^-]_0 = 1.5$ mM; $[Ce^{4+}]_0 = 3$ mM; $[H^+]_0 = 1.75$ M.

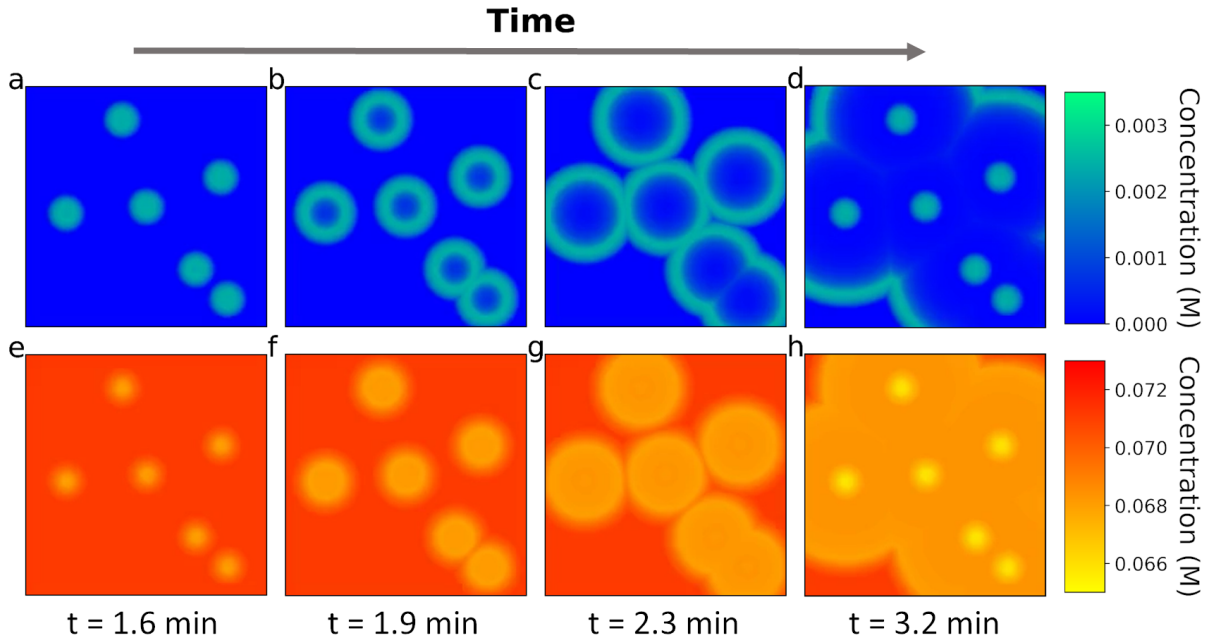

Figure S12: Two-dimensional simulation of $[Ce^{4+}]$ and $[BrO_3^-]$ chemical waves (panels a,b,c,d and e,f,g,h, respectively). Representative snapshots are shown as a function of time from reaction start.

References

(1) Martini, A.; Guda, S.; Guda, A.; Smolentsev, G.; Algasov, A.; Usoltsev, O.; Soldatov, M.; Bugaev, A.; Rusalev, Y.; Lamberti, C.; Soldatov, A. PyFitit: The Software for Quantitative Analysis of XANES Spectra Using Machine-Learning Algorithms. *Comput. Phys. Comm.* **2019**, 107064.

(2) Markovsky, I. Structured low-rank approximation and its applications. *Automatica* **2008**, *44*, 891–909.

(3) György, L.; Turányi, T.; Field, R. J. Mechanistic Details of the Oscillatory Belousov-Zhabotinskii Reaction. *J. Phys. Chem.* **1990**, *94*, 7162–7170.

(4) Barzykina, I. Chemistry and Mathematics of the Belousov-Zhabotinsky Reaction in a School Laboratory. *J. Chem. Educ.* **2020**, *97*, 1895–1902.

(5) Field, R. J.; Körös, E.; Noyes, R. M. Oscillations in Chemical Systems. II. Thorough Analysis of Temporal Oscillation in the Bromate-Cerium-Malonic Acid System. *J. Am. Chem. Soc.* **1972**, *94*, 8649–8664.

(6) Sirimungkala, A.; Försterling, H.-D.; Dlask, V.; Field, R. J. Bromination Reactions Important in the Mechanism of the Belousov Zhabotinsky System. *J. Phys. Chem. A* **1999**, *103*, 1038–1043.

(7) Barragán, D.; Ágreda, J.; Parra, W. Entropy Production in the Oregonator Model Perturbed in a Calorimeter with a Chemical Pulse. *J. Therm. Anal. Calorim.* **2015**, *119*, 705–713.

(8) Berenstein, I.; Beta, C. Cross-Diffusion in the Two-Variable Oregonator Model. *Chaos* **2013**, *23*, 033119.

(9) Pullela, S. R.; Cristancho, D.; He, P.; Luo, D.; Hall, K. R.; Cheng, Z. Temperature

Dependence of the Oregonator Model for the Belousov-Zhabotinsky Reaction. *Phys. Chem. Chem. Phys.* **2009**, *11*, 4236–4243.

(10) Aller Pellitero, M.; lvarez Lamsfus, C.; Borge, J. The Belousov-Zhabotinskii Reaction: Improving the Oregonator Model with the Arrhenius Equation. *J. Chem. Educ.* **2013**, *90*, 82–89.

(11) Field, R. J.; Noyes, R. M. Oscillations in Chemical Systems. IV. Limit Cycle Behavior in a Model of a Real Chemical Reaction. *J. Chem. Phys.* **1974**, *60*, 1877–1884.

(12) Ai, J.; Zhai, C.; Sun, W. Study on the Formation of Complex Chemical Waveforms by Different Computational Methods. *Processes* **2020**, *8*, 393.

(13) Zhao, J.; Zhang, T.; Corless, R. M. Convergence of the Compact Finite Difference Method for Second-Order Elliptic Equations. *Appl. Math. Comput.* **2006**, *182*, 1454–1469.

(14) Ai, J.; Sun, W.; Zhai, C. In *29th European Symposium on Computer Aided Process Engineering*; Kiss, A. A., Zondervan, E., Lakerveld, R., zkan, L., Eds.; Computer Aided Chemical Engineering; Elsevier, 2019; Vol. 46; pp 853–858.